

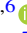










# Proposed Lunar Measurements of $r$ -Process Radioisotopes to Distinguish the Origin of Deep-sea $^{244}\text{Pu}$

Xilu Wang (王夕露)<sup>1,2,3,12</sup>, Adam M. Clark<sup>3</sup>, John Ellis<sup>4,5,6</sup>, Adrienne F. Ertel<sup>7,8</sup>, Brian D. Fields<sup>7,8,9</sup>, Brian J. Fry<sup>10</sup>, Zhenghai Liu<sup>7,8</sup>, Jesse A. Miller<sup>7,8,11</sup>, and Rebecca Surman<sup>3,12</sup>

<sup>1</sup> Key Laboratory of Particle Astrophysics, Institute of High Energy Physics, Chinese Academy of Sciences, Beijing, 100049, People's Republic of China  
[wangxl@ihep.ac.cn](mailto:wangxl@ihep.ac.cn), [xlwang811@gmail.com](mailto:xlwang811@gmail.com)

<sup>2</sup> Department of Physics, University of California, Berkeley, CA 94720, USA

<sup>3</sup> Department of Physics, University of Notre Dame, Notre Dame, IN 46556, USA

<sup>4</sup> Theoretical Physics and Cosmology Group, Department of Physics, King's College London, London WC2R 2LS, UK  
<sup>5</sup> NICPB, Rävala pst. 10, 10143 Tallinn, Estonia

<sup>6</sup> Theoretical Physics Department, CERN, CH-1211 Geneva 23, Switzerland

<sup>7</sup> Department of Astronomy, University of Illinois, Urbana, IL 61801, USA

<sup>8</sup> Illinois Center for the Advanced Study of the Universe, University of Illinois, Urbana, IL 61820, USA

<sup>9</sup> Department of Physics, University of Illinois, Urbana, IL 61801, USA

<sup>10</sup> Department of Physics, United States Air Force Academy, Colorado Springs, CO 80840, USA

<sup>11</sup> Center for Space Physics, Department of Astronomy, Boston University, Boston, MA 02215, USA

Received 2022 October 21; revised 2023 February 16; accepted 2023 February 22; published 2023 May 12

## Abstract

$^{244}\text{Pu}$  has recently been discovered in deep-sea deposits spanning the past 10 Myr, a period that includes two  $^{60}\text{Fe}$  pulses from nearby supernovae.  $^{244}\text{Pu}$  is among the heaviest  $r$ -process products, and we consider whether it was created in supernovae, which is disfavored by nucleosynthesis simulations, or in an earlier kilonova event that seeded the nearby interstellar medium with  $^{244}\text{Pu}$  that was subsequently swept up by the supernova debris. We discuss how these possibilities can be probed by measuring  $^{244}\text{Pu}$  and other  $r$ -process radioisotopes such as  $^{129}\text{I}$  and  $^{182}\text{Hf}$ , both in lunar regolith samples returned to Earth by missions such as Chang'e and Artemis, and in deep-sea deposits.

*Unified Astronomy Thesaurus concepts:* [R-process \(1324\)](#); [Supernovae \(1668\)](#); [Lunar regolith \(2315\)](#); [Compact binary stars \(283\)](#); [Mass spectrometry \(2094\)](#)

## 1. Introduction

Measurements of live radioactive isotopes can provide insights into recent astrophysical explosions such as core-collapse supernovae (SNe) within  $\mathcal{O}(100)$  pc of Earth (Ellis et al. 1996) that are expected to occur every few million years, clarifying the possibility of rarer events within  $\mathcal{O}(10)$  pc that might have caused mass extinctions in the past (Ruderman 1974; Ellis & Schramm 1995). Many experiments over the past two decades have detected pulses of live  $^{60}\text{Fe}$  in deep-sea deposits (Knie et al. 1999, 2004; Fitoussi et al. 2008; Ludwig et al. 2016; Wallner et al. 2016, 2020) from between 2 and 3 Myr ago (Mya), very likely due to a nearby core-collapse SN. There have also been measurements of  $^{60}\text{Fe}$  in the lunar regolith (Fimiani et al. 2016), in cosmic rays (Binns et al. 2016), and in Antarctic snow (Koll et al. 2019).

These measurements were accompanied by some tantalizing hints of deep-sea  $^{244}\text{Pu}$  (Paul et al. 2001; Wallner et al. 2004; Raisbeck et al. 2007; Wallner et al. 2015). These are interesting because the  $^{244}\text{Pu}$  is produced exclusively by the astrophysical rapid neutron-capture process ( $r$ -process), which is one of the dominant avenues to synthesize elements heavier than iron in the universe (Burbidge et al. 1957). The nature of the  $r$ -process lies at the heart of multimessenger astronomy, with connections

to gravitational-wave observations and gamma-ray bursts (Abbott et al. 2017a; Cowperthwaite et al. 2017; Abbott et al. 2017b; Kasen et al. 2017), as well as observations of the most ancient stars (Roederer & Lawler 2012; Holmbeck et al. 2018; Placco et al. 2020). The nuclear physics of the  $r$ -process demands that an intense neutron flux act over a short timescale  $\sim 1$  s; this points to explosive conditions (Burbidge et al. 1957). The astrophysical sites that most plausibly host such conditions are core-collapse SNe and neutron-star mergers (kilonovae (KNe)); see the reviews by Cowan et al. (1991), Arnould et al. (2007), Cowan et al. (2021), Kajino et al. (2019), and references therein. Which of these dominated production in the early Galaxy, and which dominates today, remains frustratingly difficult to identify unambiguously, in part because  $r$ -process observables such as abundance patterns potentially sum contributions from multiple events.

Deep-sea samples open a new window into the  $r$ -process and are particularly exciting because they give information on specific isotopes (not elemental sums), and they sample ejecta from specific events (Wang et al. 2021). Comparing the early solar system abundance of  $^{244}\text{Pu}$  with the deep-sea sediments from Wallner et al. (2015), Hotokezaka et al. (2015) inferred that the measured  $^{244}\text{Pu}$  came from rare  $r$ -process events. Motivated by these hints, in an earlier paper we studied possible signatures of rare SN and KN  $r$ -process events, analyzing the potential implications of  $^{244}\text{Pu}$  detection, estimating the strengths of other  $r$ -process radioisotope signatures, and discussing how they could help distinguish between potential sites (Wang et al. 2021).

<sup>12</sup> N3AS Collaboration.



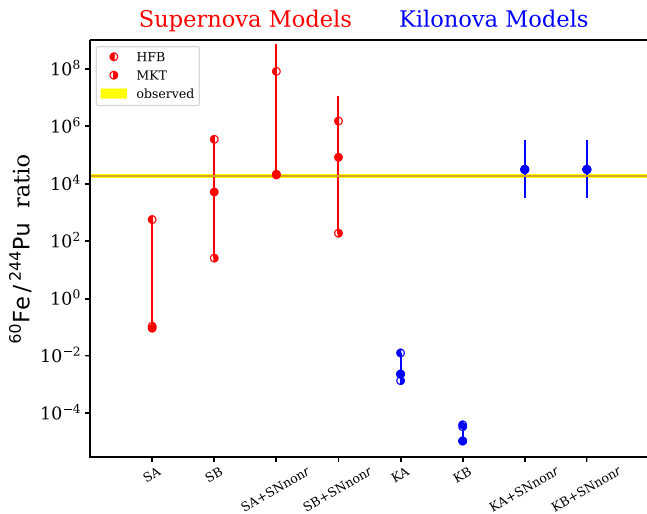


**Figure 1.** The  $^{60}\text{Fe}/^{244}\text{Pu}$  abundance ratios calculated (Wang et al. 2021) in forced  $\nu$  wind and MHD SN models (SA and SB) and in KN models (KA and KB). We present results for each model both without and including an additional non- $r$ -process SN source of  $^{60}\text{Fe}$  at 100 pc; calculations are for events 3 Mya but with a 10 Mya kilonova in the two-step KA/B+SNnonr models. The yellow band indicates the observed  $^{60}\text{Fe}/^{244}\text{Pu}$  ratio (Wallner et al. 2021) for 3 Mya (SN Plio). The error bars indicating the impact  $r$ -process nuclear uncertainties discussed in Appendix A: Filled symbols are the baseline FRDM+QRPA nuclear model, while the left (right) half-filled symbols are the HFB (MKT) models.

A major advance in studies of live astrophysical radioisotopes has recently been made by Wallner et al. (2021) with the discovery of  $^{244}\text{Pu}$  in deep-sea ferromanganese (Fe-Mn) crusts from periods that include both this and the  $\sim 3$  Mya  $^{60}\text{Fe}$  pulse. Whereas earlier hints had reported single  $^{244}\text{Pu}$  atoms, Wallner et al. (2021) reported  $181 \pm 19$  atoms above background, indicating a firm detection. This same study also found an earlier  $^{60}\text{Fe}$  pulse  $\sim 7$  Mya. These results add new dimensions to our picture of recent near-Earth explosions and widen the scope of their implications. Broadly, the detection of  $^{244}\text{Pu}$  is not only the second firmly detected radioisotope in this epoch but it also demands an  $r$ -process source and so probes the astrophysical site of the  $r$ -process. Further, the second  $^{60}\text{Fe}$  pulse shows that there were multiple explosions, as one would expect from massive stars that are highly clustered (Zinnecker & Yorke 2007). We thus follow Ertel et al. (2023) in referring to the event around 3 Mya as the Pliocene event (SN Plio) and the event around 7 Mya as the Miocene event (SN Mio). In this paper, we study the interpretation and potential implications of these new experimental results, focusing on the information to be gained from lunar measurements of  $r$ -process radioisotopes.

As has been shown in Fry et al. (2015), ordinary (non- $r$ -process) nucleosynthesis in core-collapse SNe provides the only plausible source of  $^{60}\text{Fe}$  observed in the two pulses. Wallner et al. (2021) concur, making this a starting point for their analysis. The question then becomes: Could either or both of these SNe also have produced the  $^{244}\text{Pu}$  or is a separate event required, presumably a KN?

The two  $^{60}\text{Fe}$  pulses require at least two distinct SNe. The  $^{244}\text{Pu}$  data were not sampled as finely in time as the  $^{60}\text{Fe}$  data but in three broad time windows including a surface layer that includes anthropogenic contamination. The two deeper layers each overlap with a  $^{60}\text{Fe}$  pulse, with similar  $^{60}\text{Fe}/^{244}\text{Pu}$  ratios, represented by the yellow band in Figure 1. The data show  $^{60}\text{Fe}$  to be much more abundant than  $^{244}\text{Pu}$  in both pulses.

Motivated by these data, Wang et al. (2021) proposed two scenarios for  $^{244}\text{Pu}$  deposition on Earth by recent nearby events: (1) *one step*, i.e., the deposition of  $^{244}\text{Pu}$  is a direct consequence of the propagation of the ejecta from the nearby explosion event; and (2) *two-step* process, in which an earlier KN ejecta propagates to and mixes into the proto-Local Bubble, followed by the relative motion of Earth and  $r$ -process-enriched dust, leading to the subsequent bombardment of  $^{244}\text{Pu}$  onto Earth. We will adopt and compare these scenarios below and also comment on the possibility of multiple KN explosions in the two-step process.

In this paper we confront the  $^{60}\text{Fe}$  and  $^{244}\text{Pu}$  data with the SN and neutron-star merger nucleosynthesis models developed in Wang et al. (2021) and explore the prospects of fresh measurements that might discriminate between possible scenarios, emphasizing the value of analyzing lunar regolith samples returned to Earth by missions such as Chang’e and Artemis.

## 2. Supernova and Kilonova Models of $^{60}\text{Fe}$ and $^{244}\text{Pu}$

The astrophysical origins of  $r$ -process elements including the actinides have been the subject of considerable debate (Cowan et al. 2021). SNe may produce the  $r$ -process either via a neutrino-driven wind or in magnetohydrodynamic (MHD) jets, but both mechanisms struggle to make actinides; see Wang et al. (2021) and references therein. If SNe are confirmed as robust sources of actinides such as  $^{244}\text{Pu}$ , the available models must have major omissions. Neutron-star mergers that lead to KN explosions, on the other hand, have been observed to produce  $r$ -process species such as lanthanides (Abbott et al. 2017a) and are expected to produce actinides (Cowan et al. 2021), though the latter has yet to be confirmed observationally (Zhu et al. 2018).

In Wang et al. (2021), we constructed four SN and KN models to examine  $r$ -process radioisotope production. Our two models featured a modified neutrino-driven wind (Arcones & Janka 2011) scenario forced to produce actinides, denoted by  $\nu^*$  (SA), and a high magnetic field MHD SN model (Mösta et al. 2018), denoted by SB, both with  $r$ -process nucleosynthesis constrained using data on the metal-poor star HD 160617 (Roederer & Lawler 2012). For neutron-star mergers, we explored two combinations of calculations of neutron-star merger dynamical ejecta (Bovard et al. 2017) and a disk  $\nu$ -driven wind (Just et al. 2015), constrained to fit data on either HD 160617 (KA) or the actinide-boost star J0954+5246 (Holmbeck et al. 2018; KB). Details of these models are found in Wang et al. (2021).

The  $^{60}\text{Fe}/^{244}\text{Pu}$  ratios for the four models of  $r$ -process production are compared to the data from Wallner et al. (2021) in Figure 1. In the SA and SB models, the  $^{60}\text{Fe}$  production is underestimated, as SNe produce  $^{60}\text{Fe}$  during hydrostatic burning phases and during the explosion (Limongi & Chieffi 2006; Sukhbold et al. 2016; Limongi & Chieffi 2018; Curtis et al. 2019), apart from any potential  $r$ -process contribution. Hence, in order to compare our models to the new data from Wallner et al. (2021), we need to consider sources of  $^{60}\text{Fe}$  within the SN event in addition to the  $r$ -process yields from Wang et al. (2021). Our procedure to do this appears in Appendix A.

We see that either of the SN models SA or SB could accommodate the (similar)  $^{60}\text{Fe}/^{244}\text{Pu}$  ratios reported by Wallner et al. (2021) in periods around 3 and 7 Mya. On the other hand, both the KN models KA and KB predict much smaller  $^{60}\text{Fe}/^{244}\text{Pu}$  ratios, even when the uncertainties are

taken into account. We therefore conclude that the  $^{60}\text{Fe}$  pulses and  $^{244}\text{Pu}$  detection cannot be due to KN explosions alone, at least as described by the models considered here.

We consider now the data of Wallner et al. (2021) on the  $^{60}\text{Fe}$  pulse from  $\sim 3$  Mya. The timing of this signal is consistent with that measured previously in  $^{60}\text{Fe}$  deposits in deep-sea sediments and crusts (Knie et al. 1999, 2004; Fitoussi et al. 2008; Ludwig et al. 2016; Wallner et al. 2016, 2020), though this peak is somewhat broader. The observed amplitude of the pulse and its duration of  $\gtrsim 1$  Myr are consistent with a model in which  $^{60}\text{Fe}$  from an SN 100 pc away is transported to Earth in dust grains via “pinball” trajectories that are deflected and trapped by a magnetic field within the SN remnant (Fry et al. 2020; Ertel et al. 2023). The pulse width indicated by the Wallner et al. (2021) measurements could also reflect smearing in the crust they study. Accordingly, we assume that this pulse was produced by a single SN.

In our SN models, we also make the economical assumption that the  $^{244}\text{Pu}$  from  $\leq 4.57$  Mya measured by Wallner et al. (2021) is also associated with SN Plio 3 Myr ago. We emphasize that observations with finer timing resolution would be needed to confirm this association, but note that many of our comments below would apply also if it were due to two or more SNe. As discussed above, the additional  $^{60}\text{Fe}$  peak discovered by Wallner et al. (2021)—see also Figure 1 of Fitoussi et al. (2008)—is likely due to another SN that occurred  $\sim 7$  Mya (SN Mio), also some  $\sim 100$  pc away. We assume that all the  $^{244}\text{Pu}$  from 4.57 to 9 Mya measured by Wallner et al. (2021) are associated with this SN explosion while emphasizing that observations with finer timing resolution would also be needed to confirm this association. Under this assumption, the  $^{244}\text{Pu}/^{60}\text{Fe}$  ratios in the ejecta of the two SNe  $\sim 3$  and  $\sim 7$  Mya are comparable within a factor of  $\sim 2$  and indistinguishable in Figure 1.

This is intriguing since simulations indicate that only very specific types of SN can make much  $^{244}\text{Pu}$  (Wang et al. 2021), in which case seeing two of them looks like a remarkable coincidence. If such an interpretation were correct, it would suggest not only that many or most SNe are  $r$ -process sites, but also that their production extends all the way to the actinides. If this could be established, standard  $\nu$ -driven wind and MHD models must have major omissions. That said, actinide production is possible in the forced neutrino wind and MHD models  $\nu^*$  (SA) and SB discussed in Wang et al. (2021).

Nevertheless, there are serious potential issues for scenarios with actinide production in many or most SNe provided by measurements of the  $r$ -process abundances in metal-poor stars. (a) It is known that  $r$ -process/Fe ratios (estimated using Eu/Fe as a proxy) vary wildly, with most stars showing low values and only a minority showing high values (Holmbeck et al. 2020). The obvious interpretation is that Fe and  $r$ -process production are decoupled. If SNe do indeed make the  $r$ -process, one possibility would be that (core-collapse) SN Fe production is highly variable. However, there are observational constraints on this from observations of SN light curves powered by  $^{56}\text{Ni}$  decay, so it seems more likely that the variations in  $r$ -process/Fe ratios are due to variations in  $r$ -process production. Another issue is that (b) searches for  $r$ -process species in metal-poor dwarf galaxies found them only in  $\sim 10\%$  (Ji et al. 2016). This strongly suggests that  $r$ -process events are much rarer than SNe. An alternative hypothesis is that the  $r$ -process material is ejected preferentially from the

dwarf galaxies, e.g., in jets, but in this case, jets would have to be features of most SNe, which is not supported by observations.

Motivated by these considerations, we proposed in Wang et al. (2021) that  $^{244}\text{Pu}$  signals could arise via a two-step process in which material deposited previously in the interstellar medium (ISM) by an earlier KN was then swept up by subsequent SN explosions.<sup>13</sup> Estimates of the KN rate in the Galaxy are compatible with a KN explosion  $\mathcal{O}(300)$  pc away that occurred  $\mathcal{O}(10)$  Mya. Accordingly, we also show in Figure 1 results from models in which the debris from a KN explosion 10 Mya is mixed with the  $^{60}\text{Fe}$  of SN Plio 3 Mya. This two-step model discussed in Wang et al. (2021) is consistent with the data shown in Figure 1 and could explain naturally the similarity between the  $^{244}\text{Pu}/^{60}\text{Fe}$  ratios in the periods covering the two  $^{60}\text{Fe}$  pulses found by Wallner et al. (2021).

We calculate abundances in the two-step models via scaling with the  $^{244}\text{Pu}$  observations. We adopt the observed interstellar  $^{244}\text{Pu}$  flux  $\Phi_{244} = 980 \text{ atoms cm}^{-2} \text{ Myr}^{-1}$  as reported in Wallner et al. (2021). We then infer the other  $r$ -process fluxes using their production ratio to  $^{244}\text{Pu}$  and assuming the dust incorporation and survival fractions are the same as those for plutonium. Finally, to compute fluence we assume that the flux results from stirring by SNe in the Local Bubble, which has continued since the KN explosion. For the explosion times, we adopt 10, 20, and 50 Myr ago.

The two-step model in Wang et al. (2021) assumes a single KN explosion produces the  $^{244}\text{Pu}$  seen in the deep-sea deposits. It is however possible that multiple such events could contribute to the signal since the abundance deposition is driven by the stochastic nature of KN explosions (Hotokezaka et al. 2015; Côté et al. 2021). Models for  $r$ -process enrichment show large fluctuations on timescales below the recurrence time for a given location, which is estimated to be  $\sim 100$ – $200$  Myr for turbulent diffusive mixing (Hotokezaka et al. 2015; Beniamini & Hotokezaka 2020). This timescale makes multiple events unlikely in the  $\sim 20$  Myr window available to Fe-Mn crusts, but not impossible.

We consider the case of multiple KNe in Appendix B. There we show that the signal from several events is a weighted average of signals from the individual events. Below we present KN model results for different explosion times spanning the plausible range, so multiple events in this window would appear as signals bracketed by the cases we show.

### 3. Deep-sea Measurements

Figure 1 suggests that the current  $^{60}\text{Fe}$  and  $^{244}\text{Pu}$  data on their own are insufficient to discriminate between the SN-only estimates and the two-step KN/SN scenario, so we consider also the possibility of observing additional SN pulses in deep-sea deposits from  $>7$  Mya. A model of the Local Bubble and  $^{60}\text{Fe}$  transport proposed in Breitschwerdt et al. (2016) and Schulreich et al. (2017) postulates 14–20 SNe in the Scorpius-Centaurus (Sco-Cen) stellar association within 300 pc over the past 13 My, among which might be progenitors for the two observed  $^{60}\text{Fe}$  pulses. Wallner et al. (2021) reported the results of  $^{60}\text{Fe}$  searches extending over the past 10 Myr, finding that

<sup>13</sup> First estimates of the possible amounts of swept-up  $^{60}\text{Fe}$  and  $^{244}\text{Pu}$  were given in Ellis et al. (1996). We note that the transport of material from a KN can be complex. For example, Amend et al. (2022) point out that if a KN explodes a few kiloparsec above the Galactic plane, the debris can take 1–10 Myr to fall on the disk.



**Table 1**

*r*-process Isotope Ratios in Forced SN Models for Explosions 3/7 Mya, Corresponding to the Known  $^{60}\text{Fe}$  Pulses, and in KN Models for Explosions 10/20 Mya, Bracketing the Formation of the Local Bubble

Radioisotope Ratio	Supernova Models				Kilonova Models			
	SA		SB		KA		KB	
	3 Mya	7 Mya	3 Mya	7 Mya	10 Mya	20 Mya	10 Mya	20 Mya
$^{60}\text{Fe}/^{244}\text{Pu}$	$9.2 \times 10^{-2}$	$3.2 \times 10^{-2}$	$5.3 \times 10^3$	$1.8 \times 10^3$	$3.7 \times 10^{-4}$	$3.0 \times 10^{-5}$	$1.7 \times 10^{-6}$	$1.4 \times 10^{-7}$
$^{93}\text{Zr}/^{244}\text{Pu}$	5.2	0.93	$8.2 \times 10^4$	$1.5 \times 10^4$	0.24	$3.6 \times 10^{-3}$	$7.7 \times 10^{-3}$	$1.2 \times 10^{-4}$
$^{107}\text{Pd}/^{244}\text{Pu}$	52	35	$1.3 \times 10^5$	$8.6 \times 10^4$	3.7	1.4	0.34	0.13
$^{129}\text{I}/^{244}\text{Pu}$	$3.2 \times 10^2$	$2.8 \times 10^2$	$1.7 \times 10^6$	$1.5 \times 10^6$	69	49	14	10
$^{135}\text{Cs}/^{244}\text{Pu}$	5.4	0.68	$1.2 \times 10^5$	$1.5 \times 10^4$	$8.7 \times 10^{-3}$	$5.5 \times 10^{-5}$	$3.7 \times 10^{-2}$	$2.4 \times 10^{-4}$
$^{182}\text{Hf}/^{244}\text{Pu}$	3.1	2.3	$4.4 \times 10^3$	$3.3 \times 10^3$	0.43	0.22	$6.9 \times 10^{-2}$	$3.5 \times 10^{-2}$
$^{236}\text{U}/^{244}\text{Pu}$	1.8	1.7	9.5	8.7	1.8	1.5	1.0	0.92
$^{237}\text{Np}/^{244}\text{Pu}$	0.66	0.18	1.6	0.43	$8.2 \times 10^{-2}$	$3.7 \times 10^{-3}$	$5.6 \times 10^{-2}$	$2.5 \times 10^{-3}$
$^{247}\text{Cm}/^{244}\text{Pu}$	0.50	0.43	0.45	0.39	0.38	0.27	0.35	0.25

the signal-to-background ratio for  $^{60}\text{Fe}$  falls to around unity for deposits from between 7 and 10 Mya. The relatively short  $^{60}\text{Fe}$  half-life of 2.6 My would make searches for earlier  $^{60}\text{Fe}$  pulses even more challenging. On the other hand, indirect evidence for earlier SNe could come from pulses of swept-up  $^{244}\text{Pu}$  in earlier deep-sea deposits, in view of its much longer half-life  $\sim 80$  My. Wallner et al. (2015) reported the results of a search for  $^{244}\text{Pu}$  extending over the past 25 Myr, finding one event from  $>12$  Mya. This event might just be background, but if not, it would correspond to a rate of deposition similar to that between 5 and 12 Mya. The more sensitive  $^{244}\text{Pu}$  results of Wallner et al. (2021) extend back to 9 Mya, and it would clearly be interesting to extend the search for an earlier  $^{244}\text{Pu}$  signal and any possible time structure.

#### 4. Additional Radioisotopes of Interest

Another, potentially more powerful, way to distinguish between the possible production scenarios is to look for other radioisotopes present alongside the  $^{60}\text{Fe}$  and  $^{244}\text{Pu}$ . Any *r*-process mechanism that produces  $^{244}\text{Pu}$  also produces many other radioisotopes, not only other actinides such as  $^{236}\text{U}$ ,  $^{237}\text{Np}$ , and  $^{247}\text{Cm}$ , but also many other radioisotopes with masses intermediate between  $^{244}\text{Pu}$  and  $^{60}\text{Fe}$ . Hence, their abundances would in general exhibit pulses coincident with the two SN  $^{60}\text{Fe}$  pulses, whether the *r*-process location is a recent, nearby SN or an earlier, more distant KN. However, the relative abundances of the peaks of different *r*-process isotopes would be affected by their lifetimes, which would help distinguish scenarios in which the *r*-process occurred at different times in the past.

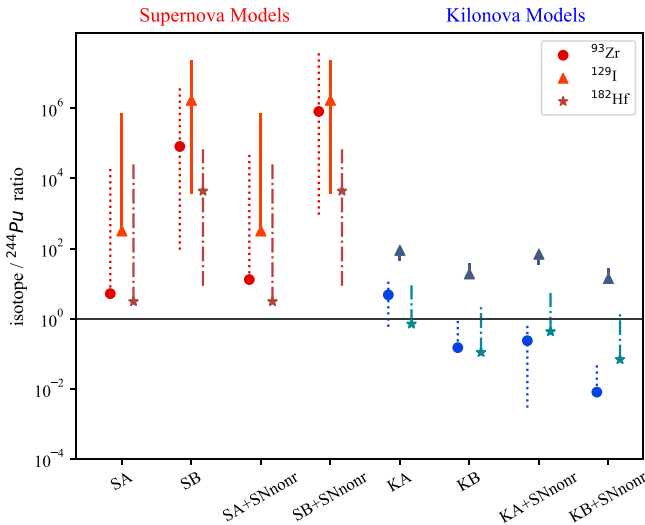
We have calculated the relative abundances of live *r*-process radioisotopes produced by the forced  $\nu$ -wind (SA) and MHD (SB) models for SN Plio and Mio that occurred 3 Mya and 7 Mya discussed above, as well as two scenarios with a KN explosion 10 or 20 Mya. If the  $^{244}\text{Pu}$  measured in Wallner et al. (2021) was produced by such an SN, one could hope to see accompanying signals of *r*-process production of the radioisotopes  $^{93}\text{Zr}$ ,  $^{107}\text{Pd}$ ,  $^{129}\text{I}$ ,  $^{135}\text{Cs}$ ,  $^{182}\text{Hf}$ ,  $^{236}\text{U}$ , and possibly  $^{237}\text{Np}$  and  $^{247}\text{Cm}$ , as listed in Table 1. The first four columns of Table 1 compare the yields of live *r*-process radioisotopes predicted by SN models SA and SB for SNe that exploded 3 and 7 Mya. We emphasize that the  $^{60}\text{Fe}/^{244}\text{Pu}$  ratios given in this table are only for  $^{60}\text{Fe}$  produced via the *r*-process and that we would expect these SNe to produce much more  $^{60}\text{Fe}$  via the standard neutron-capture mechanism. The last four columns in

Table 1 show results from calculations of *r*-process isotope production in KN models KA and KB, assuming an event 10 or 20 Mya, bracketing the formation of the Local Bubble. In this case, many of the shorter-lived radioisotopes that could have been detectable in the SN scenario would have decayed away, and we find that if the measured  $^{244}\text{Pu}$  was produced by a KN 10 or 20 Mya, the best prospect for detection (with the biggest radioisotope ratio to  $^{244}\text{Pu}$ ) is for  $^{129}\text{I}$ .

Figure 2 compares the total yields of selected live *r*-process radioisotopes predicted by our SN and KN models with direct deposition (one-step) as well as the two-step scenario (a 10 Mya KN plus a 3 Mya non-*r*-process SN), with similar calculations as in Figure 1. We highlight in Figure 2 representative isotopes in each of the three regions of the *r*-process abundance pattern, namely  $^{93}\text{Zr}$ ,  $^{129}\text{I}$ , and  $^{182}\text{Hf}$ , which we now discuss in turn.  $^{93}\text{Zr}$  can be produced in an alpha-rich freezeout of mildly neutron-rich SN ejecta without an accompanying main *r*-process, so its detection could be a probe of this additional nucleosynthetic source. Here we take the non-*r*-process SN  $^{93}\text{Zr}$  yields to be  $M_{\text{ej},93} \sim 10^{-7.5} M_{\odot}$  (see Appendix A). As for  $^{129}\text{I}$ , our predictions show that it should be detectable alongside  $^{244}\text{Pu}$  in any scenario, with measurement of the ratio offering possibly the strongest discrimination between scenarios. Finally, we anticipate that  $^{182}\text{Hf}$  could be a clear marker of prompt SN production, as it is present in potentially detectable levels for the SA and SB models, but not in the two-step KN scenarios.

It is a common feature of all the SN and KN models studied above that the best prospects for discovering a second live *r*-process radioisotope (in addition to  $^{244}\text{Pu}$ ) may be offered by  $^{129}\text{I}$ .<sup>14</sup> The  $^{129}\text{I}/^{244}\text{Pu}$  ratio calculated in the models we have studied ranges from  $\mathcal{O}(10)$  in the KN models through  $\mathcal{O}(100)$  in SN model SA to  $\mathcal{O}(10^6)$  in SN model SB, thereby offering the possibility of distinguishing between scenarios. An  $^{129}\text{I}/^{244}\text{Pu}$  ratio exceeding  $10^5$  that is coincident with either of the observed SN pulses would favor SN model SB, which would also predict  $^{182}\text{Hf}/^{244}\text{Pu}$  ratios  $>10^3$ . On the other hand, a  $^{129}\text{I}/^{244}\text{Pu}$  ratio between  $10^3$  and 10 could be accommodated by any of the models SA, KA, and KB. In this case, model SA suggests that  $^{182}\text{Hf}$  might be present at levels similar to  $^{244}\text{Pu}$ ,

<sup>14</sup> Note that iodine is volatile, and thus forms dust less readily than refractory elements, which include most other *r*-process radioisotopes of interest. (We thank Toni Wallner for pointing this out.) While the cosmic dust properties of iodine are not well known (Lodders & Fegley 2023) and merit further study, it is possible that the surviving dust fraction of  $^{129}\text{I}$  will be lower than other *r*-process elements including  $^{244}\text{Pu}$ .



**Figure 2.** Ratios to  $^{244}\text{Pu}$  of the selected live  $r$ -process radioisotopes  $^{93}\text{Zr}$ ,  $^{129}\text{I}$ , and  $^{182}\text{Hf}$ , calculated in a similar way to Figure 1. The vertical error bars indicate the impact of  $r$ -process nuclear uncertainties due to variations in masses and beta-decay rates as well as the fission yields, as discussed in Appendix A.

whereas the KN models predict smaller ratios for  $^{182}\text{Hf}$  relative to  $^{244}\text{Pu}$ , which are less likely to be detectable. Hence, the detection of  $^{182}\text{Hf}$  at a level similar to  $^{244}\text{Pu}$  would point strongly toward an SN  $r$ -process origin. Additionally, detection of any of the other  $r$ -process radioisotopes  $^{93}\text{Zr}$ ,  $^{107}\text{Pd}$ ,  $^{135}\text{Cs}$ ,  $^{182}\text{Hf}$ , and  $^{237}\text{Np}$  would favor an SN origin for the  $^{244}\text{Pu}$ . A  $^{236}\text{U}$  signal is possible in both the SN and KN scenarios but may suffer from anthropogenic or natural backgrounds in which  $^{235}\text{U}$  can capture a neutron. While  $^{247}\text{Cm}$  has no natural background, the  $^{247}\text{Cm}/^{244}\text{Pu}$  ratio is similar for SN and KN models and thus does not offer discriminating power. However, this ratio is sensitive to the unknown nuclear physics in the neutron-rich actinide region (Holmbeck et al. 2019; Lund et al. 2023), thus future  $^{247}\text{Cm}$  measurements can be used to test nuclear physics inputs, such as nuclear masses, half-lives, and fission properties.

## 5. Lunar Regolith Searches

Lunar regolith (soil) serves as a natural archive for material from nearby explosions that is complementary to terrestrial samples. Advantages of lunar archives include the geological inactivity of the Moon, the lack of an atmosphere or oceans that can redistribute material, and the lack of anthropogenic disturbances or contamination. On the other hand, the lunar surface is slowly reworked by meteoritic “gardening” (Gault et al. 1974; Costello et al. 2018), so signals from multiple events will be mixed. Moreover, the lunar surface is unshielded from cosmic rays, which create a background of radioisotopes in the regolith (Reedy & Arnold 1972; Vogt et al. 1990; Leya et al. 2001, 2021). Any SN or KN signal must stand out from this background in order to be detectable. Here we focus on the detectability of live  $r$ -process radioisotopes on the Moon.

Lunar regolith samples come at a great cost, but our inventory will soon increase dramatically beyond the Apollo and Luna samples that date back to the 1960s and 1970s. The robotic Chang’e-5 mission (Qian et al. 2021) has recently delivered a  $\sim 1.7\text{kg}$  sample from a location farther north than any prior landings, the Chang’e-6 mission will land in the

South Pole region of the Moon in 2024, and the upcoming crewed Artemis mission (Smith et al. 2020) will bring back  $\sim 100\text{ kg}$  of samples in the initial landing near the South Pole, with more planned thereafter.

We recall that the discovery of  $^{60}\text{Fe}$  in several Apollo samples was reported in Fimiani et al. (2016). The data of Wallner et al. (2021) suggest that this  $^{60}\text{Fe}$  is likely to have originated from a combination of the  $^{60}\text{Fe}$  pulses from 3 and 7 Mya, mainly the more recent pulse in view of its greater fluence and younger age. Confirmation of this  $^{60}\text{Fe}$  signal, e.g., in the sample returned recently by the Chang’e-5 mission (Qian et al. 2021) or that from a future Artemis lunar landing mission (Smith et al. 2020) would require analyzing a modest sample of  $\lesssim 100\text{ mg}$  of lunar material.<sup>15</sup>

The detection of  $^{244}\text{Pu}$  in the deep sea implies that a corresponding lunar signal must exist as well. Any cosmic-ray background for  $^{244}\text{Pu}$  must arise from the available  $^{235}\text{U}$  and  $^{238}\text{U}$  targets. These require multiple  $p$  and  $n$  captures, and even then the  $\sim 5\text{ hr}$  half-life of  $^{243}\text{Pu}$  effectively diverts any cosmogenic flow away from  $^{244}\text{Pu}$ . Cosmic rays can also destroy  $^{244}\text{Pu}$  by neutron capture, but this effect is negligible compared to decay: In Appendix C.3, we estimate  $\Gamma_{244+n} \tau_{244} \sim 4 \times 10^{-8} \ll 1$ . We therefore conclude that cosmic-ray processes do not build up any appreciable  $^{244}\text{Pu}$  background in the regolith nor do they destroy it.  $^{244}\text{Pu}$  should thus be a particularly clean lunar target, as long as return samples are protected from terrestrial contamination.

In the deep-sea Fe-Mn crust, the relative abundance of  $^{244}\text{Pu}$  reported by Wallner et al. (2021) is  $^{244}\text{Pu}/^{60}\text{Fe} \sim 5 \times 10^{-5}$ . Since it is expected that uptake on the lunar surface is as efficient as in the deep-sea case, if not more, we anticipate sample sizes of similar mass ( $\sim 10\text{ g}$ ) would be needed to discover a  $^{244}\text{Pu}$  signal.

For other, lighter  $r$ -process radioisotopes, the lunar regolith will contain a cosmogenic background that we must understand. Here we recommend the strategy that has successfully identified SN  $^{60}\text{Fe}$  in lunar regolith in the presence of a cosmic-ray background (Fimiani et al. 2016), as discussed in Appendix C.2. A radioisotope  $i$  with a potential astrophysical signal will also have a cosmogenic component, so regolith abundances will sum the two, so we write the number per unit mass as  $y_i^{\text{obs}} = y_i^* + y_i^{\text{cr}}$ . The cosmogenic background in each part of the sample will depend on the cosmic-ray flux  $\Phi$  and the local target abundance:  $y_i^{\text{cr}} \propto \Phi y_{\text{target}|i}$ , where cosmic rays produce our species via  $\text{CR} + \text{target} \rightarrow i$ . The target abundance is directly observable in the return sample, but cosmic-ray flux is not. To infer the local cosmic-ray exposure reliably requires the measurement of a radioisotope species  $j$  that is dominated by cosmic-ray production. This approach was used to measure SN-produced  $^{60}\text{Fe}$  in the lunar regolith by also measuring  $^{53}\text{Mn}$  (Fimiani et al. 2016). Such a two-radioisotope “dyadic” approach (Koll et al. 2022) is elaborated in Appendix C.2, which shows that a plot of the ratio  $y_i^{\text{obs}}/y_j^{\text{obs}}$  as a function of the ratio of cosmic-ray targets  $y_{\text{target}|i}/y_{\text{target}|j}$  falls on a line if species  $i$  is cosmogenic only, while excursions above this line would indicate the presence of an additional extrasolar component.

<sup>15</sup> Employing the regolith gardening model of Costello et al. (2018, 2020), it is estimated in Qian et al. (2021) that the depth  $\Lambda$  at which the probability of at least one overturn is 99% is  $3.45 \times 10^{-5} t_{\text{yr}}^{0.47}\text{ m}$ , where  $t_{\text{yr}}$  is the reworking time in yr. This leads to  $\Lambda = 3.8 (5.7)\text{ cm}$  for material deposited 3 (7) Mya.

**Table 2**  
Lunar Regolith  $r$ -Process Radioisotopes from Near-Earth Explosions

Isotope	Cosmic-Ray Targets	AMS Sensitivity (atoms)	Background (atoms g <sup>-1</sup> )	Sample Mass (g)	
				SN	KN
<sup>129</sup> I	Te, Ba, La	10 <sup>5</sup>	10 <sup>7</sup>	10 <sup>-1</sup> –10 <sup>3</sup>	1–10
<sup>182</sup> Hf	<sup>183</sup> W, <sup>184</sup> W, <sup>186</sup> W	10 <sup>7</sup>	3 × 10 <sup>3</sup>	2–5 × 10 <sup>5</sup>	3 × 10 <sup>3</sup> –10 <sup>6</sup>
<sup>244</sup> Pu	...	10 <sup>2</sup>	...		10

While the  $r$ -process actinide radioisotopes <sup>244</sup>Pu and <sup>247</sup>Cm will not have an appreciable cosmic-ray background, a substantial background will exist for <sup>236</sup>U and <sup>237</sup>Np, which can be created from lunar <sup>235</sup>U. Cosmogenic production will also be an issue for all of the lighter species we consider. Of the lighter species, <sup>93</sup>Zr, <sup>107</sup>Pd, and <sup>135</sup>Cs have abundant cosmogenic target nuclei in the regolith, which leads to prohibitively large backgrounds. We therefore focus on <sup>129</sup>I and <sup>182</sup>Hf where the background is smaller.

Table 2 and Figure 3 summarize the prospects for lunar detection of <sup>244</sup>Pu, as well as for <sup>129</sup>I and <sup>182</sup>Hf including cosmogenic backgrounds estimated as described in Appendix C.1. We also estimate the minimum number  $\mathcal{N}_{i,\min}$  of atoms of each species needed for a confident accelerator mass spectrometry (AMS) measurement, based on present sensitivity levels and extraction efficiency. From the needed number of atoms and the predicted number  $y_i = n_i/\rho$  of signal atoms per gram, we estimate the sample mass  $m_{i,\min} = \mathcal{N}_{i,\min}/y_i$  needed; for the SN case, this spans a large range, reflecting the large uncertainties in the predictions.

The AMS sensitivity for <sup>129</sup>I together with large <sup>129</sup>I/<sup>244</sup>Pu predicted ratios suggests that <sup>129</sup>I detection is already within the grasp of present techniques (if care is taken to avoid contamination from anthropogenic sources); indeed, intriguing measurements already exist. <sup>129</sup>I has already been detected in a Fe-Mn crust (Ji et al. 2015a), showing a dropoff with depth consistent with a background source such as natural uranium fission. The Fe-Mn crust was not independently dated, but the abundance levels appear inconsistent with the SB model while allowing room for some SA models and the KA and KB models. We note that Nishiizumi et al. (1989) used AMS to measure <sup>129</sup>I in the lunar regolith, and Nishiizumi et al. (1983) measured it in lunar rock, finding very similar abundances. Lunar rocks should not contain an SN or KN component so, at face value, these data seem to place an upper limit  $n(^{129}\text{I})/\rho \lesssim 3 \times 10^7$  atoms g<sup>-1</sup> on any extrasolar signal. This result is consistent with the indications from <sup>129</sup>I data in a Fe-Mn crust (Ji et al. 2015b) discussed in Wang et al. (2021). These measurements were not made with our research program in mind, but still, the apparent nondetection of <sup>129</sup>I puts pressure on the SN models, as seen in Figure 3: It would rule out the HFB nuclear model for the forced neutrino wind case, as well as the baseline and HFB nuclear models for the MHD SN. Future dedicated <sup>129</sup>I searches in the deep ocean and on the Moon would be of great interest.

Compared to <sup>129</sup>I, current AMS capabilities offer less promise for detecting <sup>182</sup>Hf. As estimated in Table 2, several kilograms of material may be required to detect a signal due to the limitations on AMS sensitivities caused by the interference from  $A = 182$  isobars. Due to the scarcity of available lunar material, higher sensitivity would be desirable to reduce the quantity that must be processed. Figure 3 motivates this effort, as the cosmic-ray production of <sup>182</sup>Hf is predicted to be closer

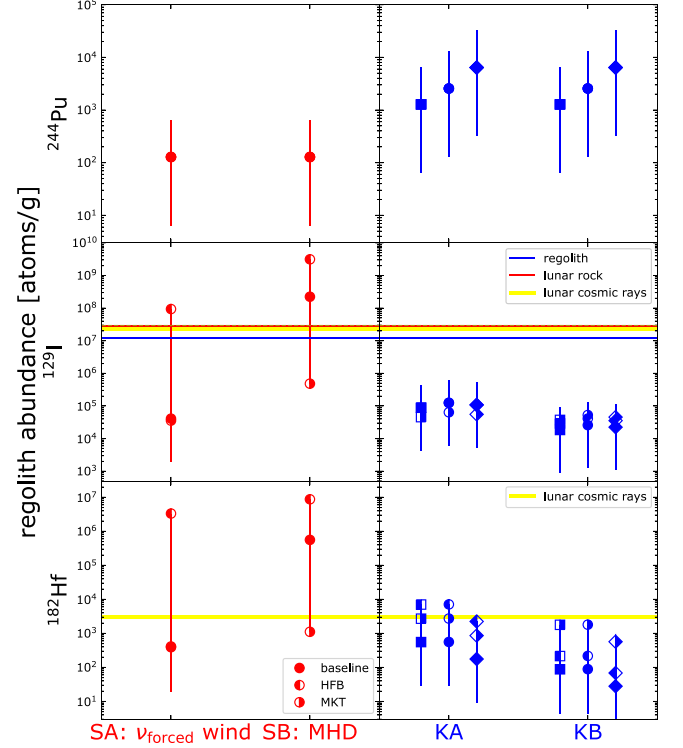


**Figure 3.** Expected abundances of select  $r$ -process radionuclides in lunar regolith, based on <sup>244</sup>Pu deep-ocean measurements. Points show predictions for SN and KN models, with error bars indicating the impact  $r$ -process nuclear uncertainties discussed in Appendix A: Filled symbols are the baseline FRDM + QRPA nuclear model, while the left (right) half-filled symbols are the HFB (MKT) models. For <sup>129</sup>I, the horizontal blue and red lines show the levels measured in Apollo samples of lunar regolith (Nishiizumi et al. 1989) and rock (Nishiizumi et al. 1983), and the yellow line shows the calculated cosmic-ray background (for details of the cosmic-ray background estimations, see Appendix C.1). SN models are for an explosion 3 Myr ago; KN models show results for explosions 10, 20, and 50 Myr ago.

to the KN predictions than that of <sup>129</sup>I. These data foreshadow the power of new radioisotope measurements on both terrestrial and lunar samples, particularly <sup>129</sup>I and <sup>182</sup>Hf, which can probe the nature of the recent explosions and of the  $r$ -process generally.

Finally, we note that the spatial distribution of <sup>60</sup>Fe and other radioisotopes on the Moon carries information about the SN direction and dust propagation (Fry et al. 2016). Over the long timescale of dust deposition, lunar rotation will average the deposition over longitude, but not latitude. Consequently, the latitude distribution of radioisotopes probes the distribution of dust arrival directions. If the dust arrives in a plane wave, there will be pronounced gradients that should be detectable, but the extant Apollo <sup>60</sup>Fe data are too uncertain to test for such a gradient (Fry et al. 2016). Future measurements of Artemis and Chang'e samples, particularly from landings near the lunar poles, could reveal the latitude distribution and thus give



unique insight into dust propagation. The results we show in Figure 3 and Table 2 are for the latitude where a plane-wave flux arrives vertically; this will be modulated by the arrival direction distribution.

## 6. Cosmic-Ray Measurements

There are also possible signatures of nearby explosions in cosmic rays, including anomalies in positron and antiproton fluxes (Kachelrieß et al. 2018), and also in the ion composition. In particular,  $^{60}\text{Fe}$  is seen in cosmic rays (Binns et al. 2016), and anomalies in elemental iron fluxes at low energies also suggest a perturbation due to a recent event (Boschini et al. 2021).

A nearby  $r$ -process event would mainly produce stable isotopes, which would be difficult to identify in deposits on Earth or Moon, but might be detectable among the cosmic rays. Searches for heavy elements in cosmic rays have led to several intriguing new results. The Cosmic Ray Isotope Spectrometer (CRIS) recently reported data on elements with atomic number  $29 \leq Z \leq 38$  and found lower abundances of  $r$ -process species than would be expected if SNe were their source (Binns et al. 2022). SuperTIGER has recently reported cosmic-ray abundances for heavier species as well (Walsh 2020; Walsh et al. 2022). The  $42 \leq Z \leq 54$  data from SuperTIGER show anomalously high abundances, i.e., exceeding the levels of a mix of 80% solar-system-like material with a 20% admixture of SN winds and ejecta that fit lower-mass cosmic-ray species. Some of these anomalous elements are produced mainly by the  $r$ -process, though with admixtures of  $s$ -process production. Intriguingly, the dominantly  $s$ -process species barium is not as enhanced as the other high- $Z$  elements, which may be circumstantial support for the hypothesis of a nearby  $r$ -process site (Walsh 2020).

Cosmic-ray measurements of other  $r$ -process species such as actinides could shed light on the nucleosynthesis pattern and thus the  $r$ -process source. If isotopic measurement were possible in future cosmic-ray experiments, the observation of  $^{182}\text{Hf}$  would be particularly interesting, since it should not have significant contamination from spallation of neighboring nuclides.  $^{129}\text{I}$  and  $^{135}\text{Cs}$  would also be of interest, though contamination from the spallation of Te, Xe, and Ba may be an issue.

There is compelling evidence that SN remnants give rise to the bulk of Galactic cosmic rays, via diffusive shock acceleration (Ackermann et al. 2013). But this same process should act in the relativistic blast waves generated in the gamma-ray bursts and KNe following neutron-star mergers, which therefore should also accelerate cosmic rays (Waxman 1995). Thus, in both the KN and SN scenarios, we expect cosmic rays to include freshly synthesized  $r$ -process material. The elemental ratios for each scenario are shaped by the prompt production as well as the spallation effects that occur as the material is ejected from the SN/KN and propagates through the ISM (Wang et al. 2020a). Whether such ratios can offer an opportunity to discriminate among scenarios requires further study.

## 7. A Strategy to Determine the Origin of Near-Earth $^{244}\text{Pu}$

By combining terrestrial and lunar measurements, we can hope to have information at least on the broad time history and overall fluence of  $^{60}\text{Fe}$  as produced in multiple SNe and

separately the time history and fluence of  $^{244}\text{Pu}$ , probably  $^{129}\text{I}$ , and possibly  $^{182}\text{Hf}$ . This will give insight into the origin of the  $r$ -process signal in radioisotopes and thus open a new window into the astrophysics site of the  $r$ -process. We distinguish three possible cases.

1. No pulse coincidence: If  $^{244}\text{Pu}$  has a time history distinct from the  $^{60}\text{Fe}$  pulses, this would point to a different origin, likely a KN that seeded the Local Bubble. Here the transport to Earth would not be coincident with the SN blasts and imply that the  $r$ -process-bearing dust moves independently in the bubble interior (as in our simple version of the two-step model). The radioisotope ratios  $r/^{244}\text{Pu}$  should follow the KN predictions, and we expect signals of  $^{244}\text{Pu}$  and longer-lived  $r$ -process radioisotopes going back to earlier times, tracing a prolonged flux back to the origin of the Local Bubble.
2. One pulse coincidence: If  $^{244}\text{Pu}$  and other  $r$ -process radioisotopes trace one (and only one) of the  $^{60}\text{Fe}$  pulses, this points to an SN origin of the  $r$ -process, and indeed an SN origin of  $r$ -process actinides. This would have major implications for SN physics and for Galactic chemical evolution. In this case, the  $^{244}\text{Pu}/^{60}\text{Fe}$  ratio would probe SN actinide production.
3. Two pulse coincidences: If  $^{244}\text{Pu}$  traces both  $^{60}\text{Fe}$  pulses, this would either (a) require that both SNe produced  $r$ -process actinides, which would challenge the prevailing SN nucleosynthesis models, or that (b) the Local Bubble was seeded with recent  $r$ -process events whose radioisotopes were later delivered by the SN blasts. This would point to a KN origin for  $r$ -process actinides. As we have shown, radioisotope ratios,  $r/^{244}\text{Pu}$ , can distinguish these cases.

High measured  $r/^{244}\text{Pu}$  ratios would indicate SN origins as in (a). This would be quite unexpected, as it would require that the Local Bubble harbored at least two  $r$ -process SNe, and these were among the nearest events, suggesting that SNe produce the  $r$ -process much more commonly than has been thought. The  $^{60}\text{Fe}/^{244}\text{Pu}$  and  $^{129}\text{I}/^{182}\text{Hf}/^{244}\text{Pu}$  ratios would probe the uniformity of the  $r$ -process synthesis in these two explosions.

Lower  $r/^{244}\text{Pu}$  ratios would point to a KN scenario as in (b). The two SNe could have different  $^{60}\text{Fe}$  yields, so the two  $r/^{60}\text{Fe}$  ratios could vary (although Wallner et al. 2021 find that  $^{60}\text{Fe}/^{244}\text{Pu}$  is consistent with a constant ratio). But the common origin of the  $r$ -process species means that the ratios among the  $r$ -process species should be the same (within errors) for the two pulses. Thus, consistency of the  $^{129}\text{I}/^{182}\text{Hf}/^{244}\text{Pu}$  ratios would provide a check on this scenario. Note also that these ratios should be similar in the no-pulse scenario above, and here too we predict signals of  $^{244}\text{Pu}$  at earlier times prior to SN Mio 7 Myr ago; both of these are hallmarks of the KN origin. Thus, the difference in the  $r$ -process deposition history between the zero and two-pulse pictures would serve as a probe of transport of KN debris within the Local Bubble.

In all cases, the  $r/^{244}\text{Pu}$  ratios probe in detail the nucleosynthesis and dust formation of these species. If the dust formation properties are similar, then these species probe the  $r$ -process pattern in the source identified by the time history results. In particular,  $^{129}\text{I}$  probes the production of the second  $r$ -process

peak, while  $^{182}\text{Hf}$  probes the base of the third peak. Observational data linking the second and third  $r$ -process peaks from the same source are limited, in large part because second-peak elements such as Te can only be spectroscopically identified in the UV. There are hints in these data that Te production may be more strongly correlated with the first  $r$ -process peak than the third (Roederer et al. 2022). A coincident detection of  $^{129}\text{I}$  and  $^{182}\text{Hf}$ , therefore, would add to this limited body of data and offer an independent test of this intriguing suggestion.<sup>16</sup>

It is worth noting that, as we have seen, the one reported measurement of  $^{129}\text{I}$  in lunar regolith (Nishiizumi et al. 1989) apparently rules out much of the SN parameter space. This is also apparently the case for the one reported  $^{129}\text{I}$  measurement in deep-ocean Fe-Mn crusts (Ji et al. 2015b; Wang et al. 2021), though the crust has not been independently dated. These tantalizing past results were not made with our research program in mind, and follow-up measurements are in order to confirm these hints and to better illuminate cosmogenic backgrounds. But the results in hand show that the experimental sensitivity to  $^{129}\text{I}$  already within reach can enable dedicated measurements to shed new light on the  $r$ -process.

## 8. Discussion: Connection with Early Solar System Radioactivities

There is a close parallel between the study of live radioisotopes from recent nearby explosions and the study of extinct early solar system (ESS) radioactivities found in meteorites (see, e.g., Huss et al. 2009; Dauphas & Chaussidon 2011; Lugaro et al. 2018; Davis 2022). Many of the central issues are identical. In both cases, a nearby explosion leaves a signature in the form of a small isotope anomaly that is detectable with the aid of sophisticated laboratory techniques. Interpreting the detections requires a model for radioisotope nucleosynthesis, transport, and sequestration in the final sample, and the implications are broad, including probes of nucleosynthesis and SN interactions with their environment.

Of course, the two situations also have important differences, which tend to make their strengths and weaknesses complementary. In the case of recent nearby explosions, the signals are resolved in time, so that multiple events can be distinguished. Also, the solar system remains in the environment that hosted the explosions, so that local astronomical observations probe its properties. Moreover, the conditions of the solar system at the time of radioisotope injection are surely similar to today and thus fairly well understood. However, the recent signals in geological samples are smaller than ESS anomalies, requiring AMS, and thus only accessible in a small number of laboratories. In the case of ESS radioisotopes, the relatively larger isotope ratios allow for more measurements and thus a wide array of species can be searched for and found, bringing to bear the power of multiple isotope ratios. On the other hand, the nature of the pre-solar nebula, and its larger environment, are not directly observable and thus are more uncertain.

ESS studies have found evidence for  $r$ -process species including not only  $^{129}\text{I}$  and  $^{247}\text{Cm}$  but also  $^{244}\text{Pu}$  (found via its

spontaneous fission products in the form of xenon isotope anomalies in Turner et al. 2007). The ESS radioisotope inventory thus includes both  $^{60}\text{Fe}$  and  $^{244}\text{Pu}$ , in close parallel to the deep-sea results. Because of these similarities, progress in studies of recent and ESS nearby events can and should be linked. Indeed, as we have seen, the detection of  $^{244}\text{Pu}$  in both cases places important and complementary constraints on the  $r$ -process. And both studies have a close interplay with models for radioisotope production and mixing on local and Galactic scales (e.g., Hotokezaka et al. 2015; Fujimoto et al. 2018; Lugaro et al. 2018; Côté et al. 2019, 2021; Fujimoto & Nagakura 2021). We urge that these connections be explored more deeply in the future.

## 9. Conclusion: Unearthing the Origin of $r$ -Process Radioisotopes

The combination of lunar and deep-sea probes of radioisotopes are complementary and may reveal their origin.

1. Deep-sea crusts characterize the broad time history, e.g., the number of  $^{60}\text{Fe}$  pulses. Future  $^{244}\text{Pu}$  measurements with better time resolution can test the coincidence with  $^{60}\text{Fe}$  and probe for events  $\gtrsim 8$  Myr ago. Searches for other  $r$ -process species test the SN and KN models, and the  $^{129}\text{I}$  radioisotope has already been found in one crust.
2. Deep-sea sediments give high-resolution time history, determining the timescales and, with improved sensitivity, the time profiles of the pulses.
3. Lunar measurements avoid anthropogenic contamination, and so would offer important confirmation of the  $^{244}\text{Pu}$  detections, and are complementary to deep-sea crusts as sites for other  $r$ -process species that can discriminate between the SN and KN scenarios. But regolith abundances require careful accounting for cosmic-ray production via measurements of target abundances and accompanying cosmogenic-dominated radioisotopes that encode exposure doses.
4. Lunar surface density measurements give the total fluence at Earth, summing over all events and avoiding uncertainties associated with terrestrial uptake factors.
5. The lunar depth profile combined with a gardening model can give timing information or, vice versa, its combination with sediment data would give a new constraint on gardening. It is possible that the depth profile might give indications of multiple events, but local stochastic variations might make this difficult.
6. Comparing the  $^{60}\text{Fe}/^{244}\text{Pu}$  and  $r/^{244}\text{Pu}$  in deep-sea crusts and sediments probes uptake and helps determine the fluence independently of the lunar measurements.
7. Comparing the lunar  $^{60}\text{Fe}/^{244}\text{Pu}$  and  $r/^{244}\text{Pu}$  with those in crusts probes uptake, and comparison with sediment data probes nonuniformity of terrestrial deposition and possibly lunar impact losses and thus impactor velocity.

The models that indicate  $>10$  SNe formed the Local Bubble (Breitschwerdt et al. 2016; Schulreich et al. 2017) suggest that there may be pulses of radioisotopes still earlier than SN Mio at 7 Myr ago. This regime is probably beyond the reach of  $^{60}\text{Fe}$  due to decay, but fortunately, all of  $^{129}\text{I}$ ,  $^{182}\text{Hf}$ , and  $^{244}\text{Pu}$  can probe to 10 Myr ago and earlier, so any early  $r$ -process signal would remain. To search for a correlation with SNe would require a long-lived radioisotope likely made in core collapse;  $^{146}\text{Sm}$  could be a candidate. The implications of

<sup>16</sup> Future searches for radioactive decay lines from  $r$ -process radioisotopes by next-generation MeV gamma-ray observatories such as COSI (<https://cosi.ssl.berkeley.edu>), AMEGO (<https://asd.gsfc.nasa.gov/amego/>), and MeVGRO (<https://indico.icranet.org/event/1/contributions/777/>) may also provide information on near-Earth nucleosynthesis events (e.g., Wang et al. 2020b).



such events are broad, with consequences for the heliosphere (Fields et al. 2008; Miller & Fields 2022; Miller et al. 2022) and possibly for the biosphere (Ruderman 1974; Hartmann et al. 2002; Melott et al. 2004, 2019). Other astrophysical observables include searches for nearby neutron stars whose location and kinematics point to a Local Bubble origin (Tetzlaff et al. 2010; Neuhäuser et al. 2020; Lin et al. 2023; Zheng et al. 2022).

The studies recommended in this work capitalize on recent technical advances, including expanded capabilities at AMS facilities to perform high-resolution measurements and the promise of next-generation radioactive beam facilities to reduce the considerable nuclear physics uncertainties of nucleosynthetic yield estimates (Mumpower et al. 2016; Horowitz et al. 2019; Schatz et al. 2022). We look forward to future studies of the deep-ocean crust—including more data on the 7 Mya SN Mio and earlier samples—as well as further data from sediments and the Antarctic snow. As we have argued here, lunar samples offer a unique complement to terrestrial sources and hold the promise to distinguish among  $r$ -process production scenarios, for which we anticipate results from the sample return missions of Chang’e and Artemis.

We are grateful for illuminating discussions with Terri Brandt and Brian Rauch about SuperTIGER and cosmic rays, and to Toni Wallner and Dominik Koll for discussions of their work. X. W., R.S., and B.D.F. acknowledge many useful discussions in the INT-21-3 workshop on cosmic radioisotopes sponsored by the Institute for Nuclear Theory. The work of X.W. was supported by the US National Science Foundation (NSF) under grant Nos. PHY-1630782 and PHY-2020275 for the Network for Neutrinos, Nuclear Astrophysics, and Symmetries (N3AS) and by the Heising-Simons Foundation under award 00F1C7. The work of A.M.C. was supported by the US Nuclear Regulatory Commission Award 31310019M0037 and the National Science Foundation under grant No. PHY-2011890. The work of J.E. was supported partly by the United Kingdom STFC Grant ST/T000759/1 and partly by the Estonian Research Council via a Mobilitas Pluss grant. The work of A. F.E. and B.D.F. was supported by the NSF under grant No. AST-2108589. The work of J.A.M. was supported by the Future Investigators in NASA Earth and Space Science and Technology (FINESST) program under grant No. 80NSSC20K1515. The work of R.S. was supported by N3AS as well as the US Department of Energy under contract Nos. DE-FG02-95-ER40934 and LA22-ML-DE-FOA-2440. R.S. also acknowledges the Aspen Center for Physics, which is supported by NSF grant PHY-2210452.

*Software:* Matplotlib (Hunter 2007), Numpy (Oliphant 2006; van der Walt et al. 2011), Portable Routines for Integrated nucleoSynthesis Modeling (PRISM) (Mumpower et al. 2018; Sprouse et al. 2021).

## Appendix A

### Nucleosynthetic Yield Estimates and Predicted Ratios of Radioisotopes

The measured ratios of  $^{60}\text{Fe}/^{244}\text{Pu}$  and other radioisotopes reflect the interstellar fluence ratios for these species. For species of SN origin such as  $^{60}\text{Fe}$ , we use the usual expression (Ellis et al. 1996; Fry et al. 2015) for fluence (i.e., the time-integrated flux),  $\mathcal{F}_{60} = f_{\text{Fe}} M_{\text{ej},60} e^{-t/\tau_{60}} / (4\pi A_{60} m_{\text{u}} r_{\text{SN}}^2)$ , in the case of  $^{60}\text{Fe}$  and similarly for other species. Here the dust

fraction measures the portion of the  $^{60}\text{Fe}$  ejecta arriving in grains. For the fluence of an individual species, one must specify the dust fraction as well as the distance, but ratios of SN species are independent of distance; they depend only on the dust fractions and yields as well as basic nuclear properties:

$$\frac{\mathcal{F}_i}{\mathcal{F}_j} = \frac{A_j f_i M_{\text{ej},i}}{A_i f_j M_{\text{ej},j}} \exp[-t_i(\tau_i^{-1} - \tau_j^{-1})] \quad (\text{A1})$$

Throughout we take  $f_i/f_j = 1$ , i.e., we assume the same dust incorporation efficiency for all species of interest. Thus, for the SN (one-step) case, the ratios depend only on the yields. For the KN case, we use the two-step model from Wang et al. (2021), with a KN distance of 1000 pc.

Our  $r$ -process nucleosynthesis calculations are made using the nuclear reaction network code Portable Routines for Integrated nucleoSynthesis Modeling (PRISM) (Mumpower et al. 2018; Sprouse et al. 2021), as implemented in Wang et al. (2021), with baseline nuclear data from Möller et al. (2016, 2019; FRDM+QRPA), and variations in the masses (Goriely et al. 2009; HFB),  $\beta$ -decay rates (Marketin et al. 2016; MKT), and fission yields (Kodama & Takahashi 1975).

To combine the  $r$ -process  $^{60}\text{Fe}$  with the ordinary SN production requires that we specify the  $^{60}\text{Fe}$  mass yields for both ordinary and  $r$ -process synthesis. Turning first to SN yields, gamma-ray line observations provide an observational indication of the mean  $^{60}\text{Fe}$  yield. Given a Galactic steady-state  $^{60}\text{Fe}$  mass  $M_{60,\text{ss}} = 2.85 M_{\odot}$  (Diehl et al. 2021) and a core-collapse SN rate  $R_{\text{SN}} = 1.7$  events/century (Rozwadowska et al. 2021), the mean  $^{60}\text{Fe}$  yield is  $M_{\text{ej},60} = M_{60,\text{ss}}/\tau_{60} R_{\text{SN}} = 4.5 \times 10^{-5} M_{\odot}$ , where  $\tau_{60}$  is the  $^{60}\text{Fe}$  lifetime; the uncertainty in this mean yield is at least a factor of 2. However, nucleosynthesis calculations suggest that  $^{60}\text{Fe}$  yields from individual SNe span a wide range, varying sensitively and nonmonotonically with progenitor mass. Yields in Sukhbold et al. (2016) span  $(4 \times 10^{-6}, 3 \times 10^{-4}) M_{\odot}$ , a range that includes the results from calculations of Limongi & Chieffi (2018) and model w of Curtis et al. (2019). We thus adopt an “ordinary”  $^{60}\text{Fe}$  yield of  $M_{\text{ej},60} = 10^{-4.5 \pm 1} M_{\odot}$ . The models labeled “SA+SNnonr” and “SB+SNnonr” in Figure 1 include this  $^{60}\text{Fe}$  yield. Similarly, the yields of  $^{93}\text{Zr}$  from ordinary (non- $r$ -process) SN explosions are in the range  $(1.4 \times 10^{-9}, 2.4 \times 10^{-7}) M_{\odot}$  (Limongi & Chieffi 2018; Curtis et al. 2019), thus an “ordinary”  $^{93}\text{Zr}$  yield of  $M_{\text{ej},93} = 10^{-7.5 \pm 1} M_{\odot}$  is included in the models labeled “SA+SNnonr” and “SB+SNnonr” in Figure 2.

For the  $r$ -process mass yields, we adopt Wang et al.’s (2021) estimate for both the SN and KN models:  $M_{\text{ej},r}(\text{SA, SB, KA, KB}) = (1.37 \times 10^{-5}, 3.0 \times 10^{-2}, 1.76 \times 10^{-2}, 7.00 \times 10^{-3}) M_{\odot}$ . The  $^{244}\text{Pu}$  and  $^{60}\text{Fe}$   $r$ -process mass yields are then  $M_{\text{ej},244} = A_{244} Y_{244} M_{\text{ej},r}$ ,  $M_{\text{ej},60} = A_{60} Y_{60} M_{\text{ej},r}$ . We add the two  $^{60}\text{Fe}$  yields for the SN models.

For  $^{244}\text{Pu}$ , we use the observed interstellar  $^{244}\text{Pu}$  flux (Wallner et al. 2021) to determine the fluence  $F_{244} = \Phi_{244}^{\text{interstellar}} \Delta t$ , where  $\Delta t$  is the time span of the measurement interval. The  $r$ -process contribution to  $^{60}\text{Fe}$  then follows as  $F_{60,r} = f_{\text{Fe}}/f_{\text{Pu}} (^{60}\text{Fe}/^{244}\text{Pu})_r F_{244}$ , where  $(^{60}\text{Fe}/^{244}\text{Pu})_r$  is the model abundance ratio by number calculated above. The other  $r$ -process species have fluence ratios just given by their production number ratios, again assuming dust fractions  $f_i/f_{\text{Pu}} = 1$ .

## Appendix B Radioisotope Signals for Multiple Kilonovae

In the KN scenario, we have considered the case of a single KN explosion that enriches the proto-Local Bubble with  $r$ -process radioisotopes. Here we consider the possibility of multiple nearby KNe contributing the observed signal. For simplicity—and based on expectations from KN rates—we will consider the case of two KNe, but it will be clear how the result generalizes.

The predicted radioisotope signatures are all linked to the observed  $^{244}\text{Pu}$  flux, and the predictions for other isotopes can be expressed via their ratios to  $^{244}\text{Pu}$ . Thus, we consider a radioisotope species  $A_i$  in the case of two KNe. We would measure the ratio given by the combined depositions (fluences) from the two events:

$$\left(\frac{A_i}{^{244}\text{Pu}}\right)_{\text{obs}} = \frac{\Phi_{i,1}e^{-t_1/\tau_i}\Delta t_1 + \Phi_{i,2}e^{-t_2/\tau_i}\Delta t_2}{\Phi_{244,1}e^{-t_1/\tau_{244}}\Delta t_1 + \Phi_{244,2}e^{-t_2/\tau_{244}}\Delta t_2} \quad (\text{B1})$$

$$= w_1 \left(\frac{A_i}{^{244}\text{Pu}}\right)_1 + w_2 \left(\frac{A_i}{^{244}\text{Pu}}\right)_2. \quad (\text{B2})$$

We see that the observed ratio is a weighted sum of the ratio  $(A_i/^{244}\text{Pu})_1 = (\Phi_i/\Phi_{244})_1$  for KN 1 alone and the corresponding ratio for the second event. The weightings depend on the  $^{244}\text{Pu}$  fluxes, durations, and times of the two events—that is, the weightings are the decayed plutonium fluences. Namely, we have

$$w_1 = \frac{(\Phi_{244,1}/\Phi_{244,2})(\Delta t_1/\Delta t_2)e^{-(t_1-t_2)/\tau_{244}}}{1 + (\Phi_{244,1}/\Phi_{244,2})(\Delta t_1/\Delta t_2)e^{-(t_1-t_2)/\tau_{244}}} \quad (\text{B3})$$

$$w_2 = 1 - w_1, \quad (\text{B4})$$

where the second equation simply shows that the weightings are true fractions summing to unity.

We see from Equations (B2) and (B4) that the observed two-KN signature will always lie between the results of the individual events, as one might expect. Thus, if there are two KNe at different times, say 10 and 20 Mya, then the result would interpolate between the first two points seen in the KN panels of Figure 3. We expect that our results span the likely range of possibilities, so realistic multiple-KN cases will lie between the lowest and highest points. This is also the case when there are more than two KNe.

## Appendix C The Cosmic-Ray Background of Radioisotopes in Lunar Regolith

Cosmic rays with MeV energies and above undergo reactions in the lunar regolith and produce radioisotopes. This cosmogenic component creates an irreducible background for radioisotopes produced in astrophysical explosions. Here we determine the level of this background and outline a strategy to use regolith measurements to disentangle the cosmogenic background from the SN or KN signal we seek. We also

estimate the level of destruction of SN and KN radioisotopes by cosmic-ray interactions.

### C.1. Cosmic-Ray Production of Radioisotopes in Lunar Regolith

Cosmic rays incident on the lunar regolith create showers of secondary protons and neutrons. These cascades are the most intense at depths around  $\sim(10, 30)$  cm below the surface for protons and neutrons respectively and are attenuated below (Reedy & Arnold 1972; Michel et al. 1991; Leya et al. 2001). For the 10–100 MeV energies most important for our purposes, the neutron fluxes are larger by more than an order of magnitude because neutrons do not suffer the Coulomb losses that stop the protons. These secondary particles react with regolith material to produce radioisotopes, whose abundance is a background that competes with our SN or KN signal.

For radioisotope  $i$  produced by cosmic-ray interactions of target nucleus  $j$ , the production rate per unit volume is

$$q_i = \langle \Phi_p \sigma_{pj \rightarrow i} + \Phi_n \sigma_{nj \rightarrow i} \rangle n_j = \Gamma_{j \rightarrow i}^{\text{CR}} n_j = \Gamma_{j \rightarrow i}^{\text{CR}} \frac{\rho}{A_j m_u} X_j. \quad (\text{C1})$$

This is the product of the target number density  $n_j$  and the cosmic-ray interaction rate per target  $\langle \Phi \sigma \rangle$ , with  $\Phi$  the cosmic-ray flux and  $\sigma$  the cross section for producing species  $i$ , summed over cosmic-ray protons and neutrons and averaged over the cosmic-ray spectrum in situ. We see that the cosmic-ray production is proportional to the target abundance, i.e., the mass fraction:  $q_i \propto n_j \propto \rho_j \propto X_j$ .

The production competes with the radioactive decay at a rate per volume, or activity  $a_i = n_i/\tau_i$ . The production and decay rates are driven to an equilibrium where  $a_i^{\text{eq}} = q_i$ . This state is reached over a timescale of order  $\tau_i$ , i.e., within a few Myr in our case, and so should be a good approximation for our purposes. Thus we expect the cosmogenic species to have equilibrium abundances given by  $n_i^{\text{eq}} = q_i \tau_i$ .

Because cosmic-ray production is proportional to the target abundance, cosmogenic radioisotope measurements are often reported as a decay rate per target mass, i.e., the specific activity

$$\mathcal{A}_{i|j} = \frac{a_i}{\rho_j} = \frac{n_i}{\tau_i X_j \rho} \stackrel{\text{eq}}{=} \frac{\Phi \sigma}{A_j m_u}, \quad (\text{C2})$$

where  $\tau_i$  is the mean life of  $i$ , and  $X_j = \rho_j/\rho$  is the mass fraction of the target. This ratio depends only on the cosmic-ray flux in the regolith (intensity and spectrum) and the cross sections for radioisotope production. We can thus find the number of cosmogenic radioisotope atoms per unit mass as

$$\begin{aligned} \frac{n_i^{\text{CR}}}{\rho} &= \mathcal{A}_{i|j} X_j \tau_i \\ &= 5.3 \times 10^5 \text{ atoms/g} \left( \frac{X_j}{100 \text{ ppm}} \right) \left( \frac{\tau_i}{10 \text{ Myr}} \right) \\ &\quad \times \left( \frac{\mathcal{A}_{i|j}}{1 \text{ dpm/kgj}} \right) \end{aligned} \quad (\text{C3})$$

where  $\text{dpm/kg}j = \text{decay min}^{-1} (\text{kg } j)^{-1}$ . Note that a mass fraction of 1 ppm corresponds to  $X(1 \text{ ppm}) = 10^{-6}$ , so our fiducial value in Equation (C3) is for  $X(100 \text{ ppm}) = 10^{-4}$ .

We can use Equation (C3) to infer the cosmic-ray backgrounds for our radioisotopes of interest and compare them with the levels we predict for the signals from nearby explosions. For example, the cosmic-ray background for  $^{129}\text{I}$  is mainly from cosmic-ray interactions with barium and tellurium isotopes. The tellurium abundance is generally small ( $X_{\text{Te}} \leq 10^{-6}$ ) in the lunar regolith, while the barium abundances in the lunar soil span  $X_{\text{Ba}} \sim 42\text{--}850$  ppm.<sup>17</sup> Adopting  $\mathcal{A}_{129\text{I}|\text{Ba}} = 1.5$  dpm/kg Ba (Schnabel et al. 2004), we estimate the cosmogenic  $^{129}\text{I}$  atoms per unit mass to be  $\sim 2.4 \times 10^7$  atoms/g, shown as the  $^{129}\text{I}$  background in Figure 3, along with values from measurements of  $^{129}\text{I}$  in a lunar rock (Nishiizumi et al. 1983) and regolith (Nishiizumi et al. 1989); for these, we use a barium mass fraction  $X_{\text{Ba}} = 389$  ppm (Schnetzler & Philpotts 1971). The background is proportional to the barium abundance and thus samples with smaller  $X_{\text{Ba}}$  would be ideal.

The main target isotope for the cosmogenic production of  $^{182}\text{Hf}$  is the tungsten isotope  $^{186}\text{W}$ . The TALYS (Koning et al. 2019)<sup>18</sup> theoretical cross-section values for cosmic rays interacting with this isotope are  $\sigma(p+^{186}\text{W}) \simeq 0.9$  mb, and  $\sigma(n+^{186}\text{W}) \simeq 2$  mb. We combine these with a tungsten regolith mass fraction of  $X_{\text{W}} = 10^{-6}$  (Kruijjer & Kleine 2017), isotope fraction  $^{186}\text{W}/\text{W} = 0.28$ , and a cosmic-ray flux in the regolith of  $\Phi_{\text{N}} = 4 \text{ cm}^{-2} \text{ s}^{-1}$ . This gives the  $^{182}\text{Hf}$  background shown as the horizontal line in Figure 3.

In general, the lunar soil will contain both an astrophysical signal from a nearby explosion (SN or KN) and a cosmogenic background. For radioisotope  $i$ , the number density in a sample  $n_i^{\text{obs}} = n_i^* + n_i^{\text{CR}}$  sums the two components, and so we have

$$\left(\frac{e_i}{\rho}\right)_{\text{obs}} = \left(\frac{n_i^*}{\rho}\right) + \left(\frac{n_i^{\text{CR}}}{\rho}\right) \quad (\text{C4})$$

$$= \left(\frac{\mathcal{F}_i^*}{\rho h_{\text{mix}}}\right) + \frac{\Gamma_{j \rightarrow i}^{\text{CR}} \tau_i}{A_j m_{\text{u}}} X_j \quad (\text{C5})$$

$$= \left(\frac{\mathcal{F}_i^*}{\rho h_{\text{mix}}}\right) + \mathcal{A}_{i|j} \tau_i X_j, \quad (\text{C6})$$

where the last equation assumes that the fluence  $\mathcal{F}_i^*$  of the isotope from a nearby explosion is mixed over a depth  $h_{\text{mix}}$ .

## C.2. Strategy to Distinguish the Astrophysical Signal from Background in Lunar Regolith Sample

Equation (C4) shows that a potential signal from an astrophysical explosion will be mixed with a cosmogenic background, and we thus require a means of separating these components. The available samples of lunar regolith and lunar soil show variations in elemental abundances. This suggests a simple strategy: Search for species  $i$  of interest in samples with

low target abundances  $X_j$ , and then plot  $n_i/\rho$  versus  $X_j$ . One can then find both the slope and intercept, which encode the cosmic-ray and astrophysical components, respectively. This simple approach faces the problem that regolith samples at different depths experience different mixing (Costello et al. 2018) and different cosmic-ray exposure (Reedy & Arnold 1972; Michel et al. 1991; Leya et al. 2001). This can introduce large spreads in both the slope and intercept of our linear trend of  $n_i/\rho$  versus  $X_j$ . We have verified with lunar and meteoritic data that the  $n(^{60}\text{Fe})/\rho$  versus the target  $X_{\text{Ni}}$  abundance that the observed trend is too noisy for robust inference of the astrophysical component. The uncertainties in the linear slope are large and consistent with zero.

To overcome the problem of different cosmic-ray exposures for different samples, one can measure another radioisotope in the same samples—a species that is only of cosmogenic origin. Fimiani et al. (2016) successfully adopted this approach, measuring not only  $^{60}\text{Fe}$  in lunar regolith, but also  $^{53}\text{Mn}$ , which has a high cosmogenic abundance due to the large abundance of its target nuclei such as  $^{56}\text{Fe}$ . Here we use their lunar and meteoritic data to illustrate this procedure. Our analysis elaborates the procedure discussed recently in Koll et al. (2022).

We consider two radioisotopes: one denoted by  $i$  that has or may have an SN component, e.g.,  $^{60}\text{Fe}$ ,  $^{244}\text{Pu}$ ,  $^{129}\text{I}$ , etc. The other is dominated by cosmic-ray production; we denote this by  $k$  and have in mind  $^{53}\text{Mn}$ . Thus, both species obey Equation (C4), but one has no discernible astrophysical component: We use this cosmogenic species  $k$  as the tracer. We write the number of radioisotope atoms per sample mass as  $y_i = n_i/\rho$ , so that  $y_i = y_i^{\text{CR}} + y_i^*$ , while  $y_k = y_k^{\text{CR}}$ . For the cosmic-ray components  $y_i^{\text{CR}} = \Phi_i \sigma_{j \rightarrow i} \tau_i = \tau_i \mathcal{A}_{i|j} X_j / A_j m_{\text{u}}$ , with a similar expression for species  $k$ . Using the  $^{60}\text{Fe}$  and  $^{53}\text{Mn}$  system as an example, we have

$$\frac{^{60}\text{Fe}}{^{53}\text{Mn}} = \frac{y_i}{y_k} = \frac{n_i}{n_k} \quad (\text{C7})$$

$$= \frac{\sigma_{j \rightarrow i} \tau_i}{\sigma_{\ell \rightarrow k} \tau_j} \frac{y_j}{y_{\ell}} + \frac{y_i^*}{y_k^{\text{CR}}} \quad (\text{C8})$$

$$= \frac{\sigma_{\text{Ni} \rightarrow ^{60}\text{Fe}} \tau_{60}}{\sigma_{\text{Fe} \rightarrow ^{53}\text{Mn}} \tau_{53}} \left(\frac{\text{Ni}}{\text{Fe}}\right) + \frac{1}{\Phi_{\text{Fe} \rightarrow ^{53}\text{Mn}}} \frac{^{60}\text{Fe}^*}{\text{Fe}}. \quad (\text{C9})$$

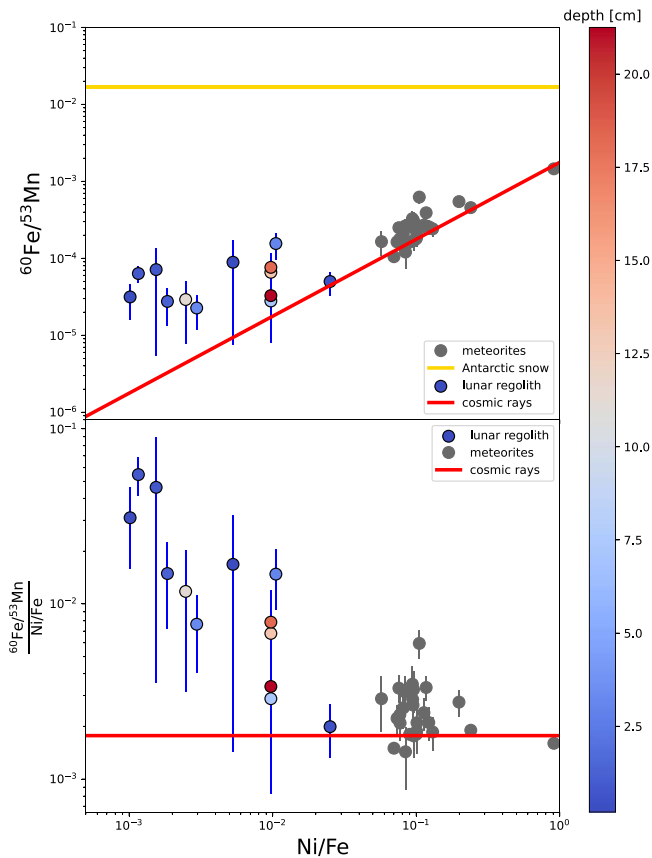
We see that a plot of  $^{60}\text{Fe}/^{53}\text{Mn}$  versus  $\text{Ni}/\text{Fe}$  should be linear with zero intercept if there is no SN component, with a slope that only depends on the ratio of the  $\sigma \tau$  values for the two species, not the cosmic-ray flux.

Figure 4 plots  $^{60}\text{Fe}/^{53}\text{Mn}$  versus  $\text{Ni}/\text{Fe}$  for both lunar regolith samples that should contain SN  $^{60}\text{Fe}$ , and for meteorites that should not (Fimiani et al. 2016; Koll et al. 2022). We see that the meteoritic data falls on a line with a nonzero slope, indicating the presence of correlated cosmogenic production of both  $^{60}\text{Fe}$  and  $^{53}\text{Mn}$ . The presence of a positive intercept points to an SN component, at a level that

<sup>17</sup> <https://www.lpi.usra.edu/lunar/samples/>

<sup>18</sup> [https://tendl.web.psi.ch/tendl\\_2021/talys.html](https://tendl.web.psi.ch/tendl_2021/talys.html)





**Figure 4.** Ratio of  $^{60}\text{Fe}/^{53}\text{Mn}$  for meteorites and lunar regolith. Panel (a): ratio of  $^{60}\text{Fe}/^{53}\text{Mn}$  vs.  $\text{Ni}/\text{Fe}$ . The linear trend for cosmic-ray production shown as a line, and the excess in regolith indicates another source. Panel (b): ratio of  $(^{60}\text{Fe}/^{53}\text{Mn})/(\text{Ni}/\text{Fe})$  vs.  $\text{Ni}/\text{Fe}$ . The cosmic-ray trend is horizontal, and the excess above it indicates the importance of an additional source.

depends on the  $^{60}\text{Fe}^*/\text{Fe}_{\text{regolith}}$  mixing of SN material in the regolith, as well as the cosmic-ray exposure  $\Phi \sigma_{53} \tau_{53}$ .

We can adapt this strategy to analyze the  $r$ -process radioisotopes with future lunar measurements. Along with these species of interest, it is important to measure at least one cosmogenic-dominated radioisotope such as  $^{53}\text{Mn}$ , but it would be of interest to measure others as well such as  $^{26}\text{Al}$ , which is abundantly produced from the spallation of silicon isotopes such as  $^{28}\text{Si}$ , as well as other examples, particularly those with lifetimes comparable to the species of interest.

Note that we have assumed that the cosmic-ray tracer species,  $^{53}\text{Mn}$  in our example, does not have an appreciable SN contribution in the regolith. In fact, SN production of  $^{53}\text{Mn}$  should occur, and Korschinek et al. (2020) report evidence for it in a Fe-Mn crust. But in this crust,  $^{53}\text{Mn}$  is still dominated by the cosmogenic component, which comes from interplanetary dust infall on Earth. We find that in a lunar sample the cosmogenic  $^{53}\text{Mn}$  signal should dominate even more because the  $^{53}\text{Mn}$  production in the regolith column will far exceed the accreted dust fluence (Love & Brownlee 1993). Thus,  $^{53}\text{Mn}$  can effectively be treated as purely of cosmic-ray origin.

### C.3. Cosmic-Ray Destruction of Radioisotopes in Lunar Regolith

Cosmic rays will also interact with the radioisotopes deposited by nearby explosions, converting them to other nuclides. This process reduces the signal we seek and so is

important to estimate. Cosmic-ray destruction of radioisotopes occurs mainly through spallation reactions.

We have examined destruction rates of  $^{60}\text{Fe}$ ,  $^{129}\text{I}$ , and  $^{244}\text{Pu}$  by cosmic-ray proton and neutron spallation on the lunar regolith. In general, the spallation (or inelastic) cross-section values for these isotopes from TALYS (Koning et al. 2019; see footnote 17) are  $\sigma_{\text{spall}} \lesssim O(10^4)$  mb at maximum, and in the regolith the cosmic-ray proton flux from 10 to 100 MeV is  $\Phi_p \lesssim O(10^{-1}) \text{ cm}^{-2} \text{ s}^{-1}$  while the neutron flux at the same energies is  $\Phi_n \lesssim O(10^0) \text{ cm}^{-2} \text{ s}^{-1}$  (Michel et al. 1991). The destruction rate is therefore at most about  $\Gamma_{\text{inel}} = (\Phi_p + \Phi_n)\sigma_{\text{inel}} \lesssim O(10^{-22}) \text{ s}^{-1}$ . This is far less than the radioactive decay rate of these isotopes  $1/\tau_i > 10^{-16} \text{ s}^{-1}$  (take  $^{244}\text{Pu}$  for example,  $\Gamma_{244+n} \tau_{244} \sim 4 \times 10^{-8} \ll 1$ ). Thus, radioactive decay overwhelmingly dominates the losses of these species, as we have assumed throughout. Consequently, the cosmic-ray destruction rates can be ignored for the lunar measurements of these isotopes.

### ORCID iDs

Xilu Wang (王夕露) <https://orcid.org/0000-0002-5901-9879>  
 Adam M. Clark <https://orcid.org/0000-0002-2881-7982>  
 John Ellis <https://orcid.org/0000-0002-7399-0813>  
 Adrienne F. Ertel <https://orcid.org/0000-0002-3876-2057>  
 Brian D. Fields <https://orcid.org/0000-0002-4188-7141>  
 Brian J. Fry <https://orcid.org/0000-0002-2786-5667>  
 Zhenghai Liu <https://orcid.org/0000-0002-8056-2526>  
 Jesse A. Miller <https://orcid.org/0000-0001-5071-0412>  
 Rebecca Surman <https://orcid.org/0000-0002-4729-8823>

### References

- Abbott, B. P., Abbott, R., Abbott, T. D., et al. 2017a, *ApJL*, 848, L12  
 Abbott, B. P., Abbott, R., Abbott, T. D., et al. 2017b, *PhRvL*, 119, 161101  
 Ackermann, M., Ajello, M., Allafort, A., et al. 2013, *Sci*, 339, 807  
 Amend, B., Zrake, J., & Hartmann, D. H. 2022, *ApJ*, 939, 59  
 Arcones, A., & Janka, H. T. 2011, *A&A*, 526, A160  
 Arnould, M., Goriely, S., & Takahashi, K. 2007, *PhR*, 450, 97  
 Beniamini, P., & Hotokezaka, K. 2020, *MNRAS*, 496, 1891  
 Binns, W. R., Israel, M. H., Christian, E. R., et al. 2016, *Sci*, 352, 677  
 Binns, W. R., Wiedenbeck, M. E., von Roseninge, T. T., et al. 2022, *ApJ*, 936, 13  
 Boschini, M. J., Della Torre, S., Gervasi, M., et al. 2021, *ApJ*, 913, 5  
 Bovard, L., Martin, D., Guercilena, F., et al. 2017, *PhRvD*, 96, 124005  
 Breitschwerdt, D., Feige, J., Schulreich, M. M., et al. 2016, *Natur*, 532, 73  
 Burbidge, E. M., Burbidge, G. R., Fowler, W. A., & Hoyle, F. 1957, *RvMP*, 29, 547  
 Costello, E. S., Ghent, R. R., Hirabayashi, M., & Lucey, P. G. 2020, *JGRE*, 125, e2019JE006172  
 Costello, E. S., Ghent, R. R., & Lucey, P. G. 2018, *Icar*, 314, 327  
 Côté, B., Eichler, M., Yague Lopez, A., et al. 2021, *Sci*, 371, 945  
 Côté, B., Lugaro, M., Reifarh, R., et al. 2019, *ApJ*, 878, 156  
 Cowan, J. J., Sneden, C., Lawler, J. E., et al. 2021, *RvMP*, 93, 015002  
 Cowan, J. J., Thielemann, F.-K., & Truran, J. W. 1991, *PhR*, 208, 267  
 Cowperthwaite, P. S., Berger, E., Villar, V. A., et al. 2017, *ApJL*, 848, L17  
 Curtis, S., Ebinger, K., Fröhlich, C., et al. 2019, *ApJ*, 870, 2  
 Dauphas, N., & Chaussidon, M. 2011, *AREPS*, 39, 351  
 Davis, A. M. 2022, *ARNPS*, 72, 339  
 Diehl, R., Lugaro, M., Heger, A., et al. 2021, *PASA*, 38, e062  
 Ellis, J., Fields, B. D., & Schramm, D. N. 1996, *ApJ*, 470, 1227  
 Ellis, J., & Schramm, D. N. 1995, *PNAS*, 92, 235  
 Ertel, A. F., Fry, B. J., Fields, B. D., & Ellis, J. 2023, *ApJ*, 947, 58  
 Fields, B. D., Athanassiadou, T., & Johnson, S. R. 2008, *ApJ*, 678, 549  
 Fimiani, L., Cook, D. L., Faestermann, T., et al. 2016, *PhRvL*, 116, 151104  
 Fitoussi, C., Raisbeck, G. M., Knie, K., et al. 2008, *PhRvL*, 101, 121101  
 Fry, B. J., Fields, B. D., & Ellis, J. R. 2015, *ApJ*, 800, 71  
 Fry, B. J., Fields, B. D., & Ellis, J. R. 2016, *ApJ*, 827, 48  
 Fry, B. J., Fields, B. D., & Ellis, J. R. 2020, *ApJ*, 894, 109  
 Fujimoto, S.-i., & Nagakura, H. 2021, *MNRAS*, 502, 2319  
 Fujimoto, Y., Krumholz, M. R., & Tachibana, S. 2018, *MNRAS*, 480, 4025

- Gault, D. E., Hoerz, F., Brownlee, D. E., & Hartung, J. B. 1974, *LPSC*, **3**, 2365
- Goriely, S., Chamel, N., & Pearson, J. M. 2009, *PhRvL*, **102**, 152503
- Hartmann, D. H., Kretschmer, K., & Diehl, R. 2002, in Proc. 11th Workshop on “Nuclear Astrophysics”, ed. W. Hillebrandt & E. Müller (Garching: Max-Planck-Institut für Astrophysik), 154
- Holmbeck, E. M., Beers, T. C., Roederer, I. U., et al. 2018, *ApJL*, **859**, L24
- Holmbeck, E. M., Hansen, T. T., Beers, T. C., et al. 2020, *ApJS*, **249**, 30
- Holmbeck, E. M., Sprouse, T. M., Mumpower, M. R., et al. 2019, *ApJ*, **870**, 23
- Horowitz, C. J., Arcones, A., Côté, B., et al. 2019, *JPhG*, **46**, 083001
- Hotokezaka, K., Piran, T., & Paul, M. 2015, *NatPh*, **11**, 1042
- Hunter, J. D. 2007, *CSE*, **9**, 90
- Huss, G. R., Meyer, B. S., Srinivasan, G., Goswami, J. N., & Sahijpal, S. 2009, *GeCoA*, **73**, 4922
- Ji, A. P., Frebel, A., Chiti, A., & Simon, J. D. 2016, *Natur*, **531**, 610
- Ji, L., Liu, G., Chen, Z., et al. 2015a, *AcOSi*, **34**, 31
- Ji, L., Liu, G., Huang, Y., Xing, N., & Chen, Z. 2015b, *AcOSi*, **34**, 13
- Just, O., Bauswein, A., Pulpillo, R. A., Goriely, S., & Janka, H.-T. 2015, *MNRAS*, **448**, 541
- Kachelrieß, M., Neronov, A., & Semikoz, D. V. 2018, *PhRvD*, **97**, 063011
- Kajino, T., Aoki, W., Balantekin, A. B., et al. 2019, *PrPNP*, **107**, 109
- Kasen, D., Metzger, B., Barnes, J., Quataert, E., & Ramirez-Ruiz, E. 2017, *Natur*, **551**, 80
- Knie, K., Korschinek, G., Faestermann, T., et al. 1999, *PhRvL*, **83**, 18
- Knie, K., Korschinek, G., Faestermann, T., et al. 2004, *PhRvL*, **93**, 171103
- Kodama, T., & Takahashi, K. 1975, *NuPhA*, **239**, 489
- Koll, D., Faestermann, T., Korschinek, G., et al. 2022, *EPJWC*, **260**, 11022
- Koll, D., Korschinek, G., Faestermann, T., et al. 2019, *PhRvL*, **123**, 072701
- Koning, A. J., Rochman, D., Sublet, J.-C., et al. 2019, *NDS*, **155**, 1
- Korschinek, G., Faestermann, T., Poutivtsev, M., et al. 2020, *PhRvL*, **125**, 031101
- Kruijjer, T. S., & Kleine, T. 2017, *E&PSL*, **475**, 15
- Leya, I., Hirtz, J., & David, J.-C. 2021, *ApJ*, **910**, 136
- Leya, I., Neumann, S., Wieler, R., & Michel, R. 2001, *M&PS*, **36**, 1547
- Limongi, M., & Chieffi, A. 2006, *ApJ*, **647**, 483
- Limongi, M., & Chieffi, A. 2018, *ApJS*, **237**, 13
- Lin, J., Li, C., Wang, W., et al. 2023, *ApJL*, **944**, L4
- Lodders, K., & Fegley, B. 2023, *ChEG*, **83**, 125957
- Love, S. G., & Brownlee, D. E. 1993, *Sci*, **262**, 550
- Ludwig, P., Bishop, S., Egli, R., et al. 2016, *PNAS*, **113**, 9232
- Lugaro, M., Ott, U., & Kereszturi, Á. 2018, *PrPNP*, **102**, 1
- Lund, K. A., Engel, J., McLaughlin, G. C., et al. 2023, *ApJ*, **944**, 144
- Marketin, T., Huther, L., & Martinez-Pinedo, G. 2016, *PhRvC*, **93**, 025805
- Melott, A. L., Lieberman, B. S., Laird, C. M., et al. 2004, *IJAsB*, **3**, 55
- Melott, A. L., Marinho, F., & Paulucci, L. 2019, *AsBio*, **19**, 825
- Michel, R., Dragovitsch, P., Cloth, P., Dagge, G., & Filges, D. 1991, *Metic*, **26**, 221
- Miller, J. A., & Fields, B. D. 2022, *ApJ*, **934**, 32
- Miller, J. A., Fields, B. D., Chen, T. Y., et al. 2022, *ApJ*, **934**, 32
- Möller, P., Mumpower, M. R., Kawano, T., & Myers, W. D. 2019, *ADNDT*, **125**, 1
- Möller, P., Sierk, A. J., Ichikawa, T., & Sagawa, H. 2016, *ADNDT*, **109**, 1
- Mösta, P., Roberts, L. F., Halevi, G., et al. 2018, *ApJ*, **864**, 171
- Mumpower, M. R., Kawano, T., & Möller, P. 2016, *PhRvC*, **94**, 064317
- Mumpower, M. R., Kawano, T., Sprouse, T. M., et al. 2018, *ApJ*, **869**, 14
- Neuhäuser, R., Gießler, F., & Hambaryan, V. V. 2020, *MNRAS*, **498**, 899
- Nishiizumi, K., Elmore, D., Honda, M., Arnold, J. R., & Gove, H. E. 1983, *Natur*, **305**, 611
- Nishiizumi, K., Kubik, P. W., Sharma, P., & Arnold, J. R. 1989, *Metic*, **24**, 310
- Oliphant, T. 2006, NumPy: A Guide to NumPy (USA: Trelgol Publishing), <http://www.numpy.org/>
- Paul, M., Valenta, A., Ahmad, I., et al. 2001, *ApJL*, **558**, L133
- Placco, V. M., Santucci, R. M., Yuan, Z., et al. 2020, *ApJ*, **897**, 78
- Qian, Y., Xiao, L., Wang, Q., et al. 2021, *E&PSL*, **561**, 116855
- Raisbeck, G., Tran, T., Lunney, D., et al. 2007, *NIMPB*, **259**, 673
- Reedy, R. C., & Arnold, J. R. 1972, *JGR*, **77**, 537
- Roederer, I. U., Cowan, J. J., Pignatari, M., et al. 2022, *ApJ*, **936**, 84
- Roederer, I. U., & Lawler, J. E. 2012, *ApJ*, **750**, 76
- Rozwadowska, K., Vissani, F., & Cappellaro, E. 2021, *NewA*, **83**, 101498
- Ruderman, M. A. 1974, *Sci*, **184**, 1079
- Schatz, H., Becerril Reyes, A. D., Best, A., et al. 2022, *JPhG*, **49**, 110502
- Schnabel, C., Leya, I., Gloris, M., et al. 2004, *M&PS*, **39**, 453
- Schnetzler, C. C., & Philpotts, J. A. 1971, *LPSC*, **2**, 1101
- Schulreich, M. M., Breitschwerdt, D., Feige, J., & Dettbarn, C. 2017, *A&A*, **604**, A81
- Smith, M., Craig, D., Herrmann, N., et al. 2020, in 2020 IEEE Aerospace Conf. (Piscataway, NJ: IEEE), 1
- Sprouse, T. M., Mumpower, M. R., & Surman, R. 2021, *PhRvC*, **104**, 015803
- Sukhbold, T., Ertl, T., Woosley, S. E., Brown, J. M., & Janka, H. T. 2016, *ApJ*, **821**, 38
- Tetzlaff, N., Neuhauser, R., Hohle, M. M., & Maciejewski, G. 2010, *MNRAS*, **402**, 2369
- Turner, G., Busfield, A., Crowther, S. A., et al. 2007, *E&PSL*, **261**, 491
- van der Walt, S., Colbert, S. C., & Varoquaux, G. 2011, *CSE*, **13**, 22
- Vogt, S., Herzog, G. F., & Reedy, R. C. 1990, *RvGeo*, **28**, 253
- Wallner, A., Faestermann, T., Feige, J., et al. 2015, *NatCo*, **6**, 5956
- Wallner, A., Feige, J., Fifield, L. K., et al. 2020, *PNAS*, **117**, 21873
- Wallner, A., Feige, J., Kinoshita, N., et al. 2016, *Natur*, **532**, 69
- Wallner, A., Froehlich, M. B., Hotchkis, M. A. C., et al. 2021, *Sci*, **372**, 742
- Wallner, C., Faestermann, T., Gerstmann, U., et al. 2004, *NewAR*, **48**, 145
- Walsh, N. E. 2020, Washington Univ. Arts & Sciences Electronic Theses and Dissertations, 2251
- Walsh, N. E., Akaike, Y., Binns, W. R., et al. 2022, *ICRC (Berlin)*, **37**, 118
- Wang, X., Clark, A. M., Ellis, J., et al. 2021, *ApJ*, **923**, 219
- Wang, X., , N3AS Collaboration, Fields, B. D., et al. 2020a, *ApJ*, **893**, 92
- Wang, X., , N3AS Collaboration, Vassh, N., et al. 2020b, *ApJL*, **903**, L3
- Waxman, E. 1995, *PhRvL*, **75**, 386
- Zheng, L.-L., Sun, M., Gu, W.-M., et al. 2022, arXiv:2210.04685
- Zhu, Y., Wollaeger, R. T., Vassh, N., et al. 2018, *ApJL*, **863**, L23
- Zinnecker, H., & Yorke, H. W. 2007, *ARA&A*, **45**, 481